Microelectronics Reliability 55 (2015) 2689–2697

Contents lists available at ScienceDirect

Microelectronics Reliability

journal homepage: www.elsevier.com/locate/mr

Microscale temperature sensing using novel reliable silicon vertical microprobe array: Computation and experiment

M.A. Matin [a,*], A. Ikedo [b], T. Kawano [b,c], K. Sawada [b,c], M. Ishida [b,c]

[a] Glass and Ceramic Engineering, Bangladesh University of Eng. and Tech. (BUET), Dhaka 1000, Bangladesh
[b] Electrical and Electronic Information Engineering, Toyohashi University of Technology (TUT), Toyohashi, Aichi 441-8580, Japan
[c] Electronics-Inspired Interdisciplinary Research Institute (EIIRIS), Toyohashi University of Technology, Toyohashi 441-8580, Japan

ARTICLE INFO

Article history:
Received 12 April 2015
Received in revised form 5 September 2015
Accepted 5 September 2015
Available online 26 September 2015

Keywords:
Reliability
Devices
Thermal modeling
Temperature sensing
Microprobe
Sensitivity

ABSTRACT

Microscale temperature sensing using a fabricated novel vertical silicon microprobe array was investigated for the first time using a combined simulation and experimental technique. In this context, silicon microprobes were designed with 3 μm in diameter and 30 μm in height. These high-aspect-ratio probes are found to be effective in microscale multisite temperature sensing. The designed microprobes (p-type) were fabricated in <111> out-of-plane orientation using vapor–liquid-solid (VLS) technique on n-type silicon substrate. The temperature dependent shift in the rectifying current–voltage (I–V) curves of the embedded p–n diode was experimentally determined and the temperature sensitivity of diode was found to be −2.3 mV/K at 0.1 μA. A complete 3-D model of the microprobe was created and finite element (FE) method was applied to compute the sensing capability by capturing temperature distribution taking anisotropic and phonon scattering effects on thermal conductivity of silicon into account. The obtained computational result on microscale temperature sensitivity has shown a similar trend of experimental findings. FE simulation thus can serve as a tool to a-priori predict temperature sensing capabilities of microprobes used in many applications such as artificial electronic fingertips of robotic hand/prosthetics, biological soft samples.

Nomenclature

a_r	Radiation cross-sectional area	m^2
c_p	Specific heat	J mole^{-1} K^{-1}
d	Diameter of the probe	m
h_c	Heat conduction coefficient	W m^{-2} K^{-1}
h_g	Heat convection coefficient	W m^{-2} K^{-1}
h_r	Radiative heat transfer coefficient	W m^{-2} K^{-1}
h_j	Contact conductance	W K^{-1}
r_c	Contact resistance	KW^{-1}
k	Thermal conductivity	W m^{-1} K^{-1}
Kn	Knudsen number	
k_B	Stefan–Boltzmann constant	J K^{-1}
Δl	Air-gap	m
N_u	Nusselt number	
Pr	Prandtl number	
p	Gas pressure	N m^{-2}
$\bar{q}_c$	Heat flux vector	W m^{-2}
r_p	Thermal resistance of probe	K W^{-1}
T	Temperature	K
ΔT	Temperature increase	K

Greek symbols

λ	The molecular mean free path	(m)
α	Accommodation coefficient	(−)
Ψ	Internal degree of freedom	(−)
ρ	Mass density	(Kg·m^{-3})

Subscripts

p	probe
sp	spreading
sub	substrate
ref	reference

1. Introduction

Miniaturized probe sensors with high sensitivity and more functionality suitable for touching and analyzing objects are in great demand in many potential applications such as artificial electronic fingertips of robotic hand/prosthetics for sensing of touch and force/temperature mapping probe arrays to investigate small materials as well as biological soft samples [1–13].

* Corresponding author.
E-mail address: matin.md.a@gmail.com (M.A. Matin).

http://dx.doi.org/10.1016/j.microrel.2015.09.003
0026-2714/

The piezoresistance effect of silicon can be exploited as one of the principles to probe force [14]. In addition, the shift in the rectifying voltage of a p–n junction has been employed to measure temperature [15].

However, the existing temperature sensing technology is confronted with a big challenge to tantalize vertical microprobes for local temperature sensing with high spatial resolution.

In this context, vertically aligned silicon (Si) microprobes can be used effectively as temperature and force sensors. In this article, we will focus only on temperature sensing using smartly designed vertical Si microprobes. If a p–n junction is incorporated into the microprobe base, the temperature of the probe will vary with the temperature of the measuring object, thereby resulting shift in I–V curves. Compared to planar sensor elements, the advantages of using Si vertical microprobes are manifolds: 1) an object is contacted only in a very small fraction of the microprobe tip, 2) it has the ability for tactile sensing to measure microscale objects such as cells and nerve tissue, 3) it can be extended as nerve potential sensors for spine neural tissue, 4) simultaneous measurement of temperature and force from allocation is possible using same sensor element, 5) the sensor elements can be arranged in several 10 μm spatial intervals thereby allowing to obtain high spatial resolution.

When there is an air-gap between the microprobe and object, the temperature sensing capability of probes is controlled by three modes of heat transfer namely conduction, convection and radiation. The dominant mode of heat transfer depends on sensing temperatures, size of device, and air-gap. If the air gap between the probe tip and W-needle is small (several microns), heat conduction in air has a dominant effect. Therefore, air-gap thermal contact resistance would play a significant role in heat conduction to probe. To conduct sensing capability of microprobe, a Tungsten (W) needle) with a constant temperature was employed in this research to mimic the object. Even when, The usefulness of the analogy between the flow of electric current and the flow of heat becomes apparent when a satisfactory description of the heat transfer at the interface of two conducting media is needed. Due to machining limitations, no two solid surfaces will ever form a perfect contact when they are pressed together. Tiny air gaps will always exist between the two contacting surfaces due to their roughness. Thus, heat flux near the interface is constricted in the microcontact regions manifesting contact resistance (see in Fig. 2). The contact resistance, r_c can be represented by the following equation

$$r_c = \frac{\Delta T}{qA_a} \tag{1}$$

where q is the heat flux (in W/m^2) and A_a is the apparent cross-sectional area (in m^2). Due to asperities, contacting interfaces are never perfectly flat, thus microscopic contact area (actual) is usually much less than macroscopic contact area (apparent, A_a). Due to deformation, contact area varies with the applied normal force between the two contacting interfaces.

However, in terms of contact conductance, contact resistance is defined as

$$r_c = \frac{1}{h_j A_a} \tag{2}$$

$$= \frac{1}{(h_c + h_r + h_g)A_a} \tag{3}$$

where contact conductance h_j is the sum of three series heat conductances namely: 1) the conduction between contacting points between two surfaces of W-needle and microprobe (h_c), 2) the radiation through the air-gap between the surfaces (h_r), and 3) the gas conduction through the air-gap (h_g). When thickness of air-gap is small, heat conduction through air-gap maybe approximated to be controlled only by heat conduction coefficient, h_g through air [16]

$$h_g = \frac{\kappa_a}{\Delta \ell} \tag{4}$$

where $\Delta\ell$ is the thickness of air-gap and κ_a is the thermal conductivity (of air).

In similar fashion, heat transfer coefficient for conduction (h_c) in material is defined as

$$h_c = \frac{\kappa}{\Delta x} \tag{5}$$

where Δx is material thickness and κ is the thermal conductivity of material.

In words, h represents the heat flow per unit area per unit temperature difference. The larger h_c is, the larger the heat transfer q.

Now, 1-D Fourier's law of continuum heat conduction reads [17]

$$q = -\kappa \frac{\partial T}{\partial x} \tag{6}$$

where q is the heat flux as mentioned before and κ is thermal conductivity.

Using conservation of energy, one may readily obtain a 1-D heat equation in simpler form without any heat source or sink

$$\frac{\partial T}{\partial t} = \alpha \frac{\partial^2 T}{\partial^2 x} \tag{7}$$

where α is the thermal diffusivity ($\alpha = \frac{\kappa}{\rho c}$), ρ is mass density and c is specific heat and ρc denotes volumetric heat capacity (ability to store heat).

However, if the characteristic length of gas layer, $\Delta\ell$ has the same order of magnitude as the molecular mean free path of gas molecules (air), (λ), the Fourier heat conduction equation breaks down and the gas begins to exhibit noncontinuum effects. The onset of noncontinuum gas rarefaction effect is typically indicated by the Knudsen number, Kn defined as the ratio of λ to $\Delta\ell$. Based on the magnitude of the Kn number, heat conduction in air can be divided into four different regimes: continuum ($Kn < 0.01$), slip i.e. temperature-jump ($0.1 > Kn > 0.01$), transition ($10 > Kn > 0.1$), and free-molecular ($Kn > 10$).

In continuum regime, the conductive heat flux, q_c in W/mm^2 is defined as [18]

$$q_c = -\frac{k_r\left(T_t^{\xi+1} - T_p^{\xi+1}\right)}{(\xi+1)T_r^{\xi}L} \tag{8}$$

where, T_t (373 K) is the source temperature (hot body) and T_r (293 K) is the reference temperature in Kelvin, T_p is the temperature of probe tip, ξ (0.770) is the temperature exponent, k_r is thermal conductivity at reference state (293 K), and L is the characteristic length of gas layer (in the first case it is 5 μm).

The conductive heat flux, q_{fm} in free-molecular regime is represented by [19]

$$q_{\mathrm{fm}} = -\left(\frac{8k_B}{\pi \mathrm{m}}\right)^{\frac{1}{2}} \frac{\alpha}{2-\alpha}\left(1 + \frac{d_f}{4}\right)\left(T_t^{1/2} - T_p^{1/2}\right)p \tag{9}$$

where, k_B (1.38066×10^{-23} J/K) is the Stefan–Boltzmann constant, m (4.27×10^{-26} kg) is gas mass, d_f (=2, considering rotation and vibration) is the internal degree of freedom, α is the accommodation coefficient (0.8 to 0.98) where a lower bound value is considered, and p (1.01325×10^5 Pa) is atmospheric gas pressure.

In *transition region*, the heat flux, q_{tr} in W/mm^2 is defined as [19]

$$q_{\mathrm{tr}} = \frac{1}{1+\left(\frac{2k_rT}{L\frac{\alpha}{2-\alpha}\left(1+\frac{d_f}{4}\right)\mathrm{cp}}\right)} q_c \tag{10}$$

where c is $(\frac{8k_BT}{\pi m})^{1/2}$.

In *temperature jump region* (*slip*) (*Kn* is calculated to be 0.0112), the heat flux, q_{tj} in W/mm^2 is defined as [19]

$$q_{tj} = \frac{1}{1+\frac{q_c}{q_{fm}}} q_c \,. \tag{11}$$

However, at micro-scale *convective heat transfer* in air is not zero though it maybe considered as secondary compared to conduction mode. The convective heat transfer coefficient, h_v can be estimated according to (for the limiting case of a horizontal cylinder immersed in air) [20]

$$h_v = \frac{N_u k_a}{d} \tag{12}$$

where d is the diameter of the probe, k_a is the thermal conductivity of air, and N_u is the Nusselt number with a value 0.36 for R_e in the range of 10^{-3} to 10^{-6} [21]. In addition, *radiation mode* heat transfer in air needs to be considered at temperatures higher than 300 °C. The radiative heat transfer coefficient (h_r) is defined as [22]

$$h_r = 4\varepsilon\sigma\frac{A_r}{A_a}\left[273.2+\frac{(T_{\mathrm{el}}+T_p)}{2}\right]^3 \tag{13}$$

where ε is the emissivity, σ is the Stefan–Boltzmann constant ($5.67\times10^{-8}W/m^2\cdot K$), A_r is the effective radiation area, A_a is the apparent contact area, T_r is the reference temperature (293 K), and T_{el} is the average temperature of contact bodies (see Fig. 2).

However, no systematic study has been conducted yet to employ both simulation and experiments to understand micro-scale heat conduction and temperature distribution in microprobe and its effect on temperature mapping.

In this paper, we thus fabricate high-density p-silicon microprobe array sensor employing IC-compatible VLS growth process. Employing Si device fabrication technology signal processing circuits and sensing elements are integrated on the same chip.

Advantage was taken due to the formation (auto embedded) of temperature sensitive p–n diode system at the junction of the p-probe and n-silicon substrate as confirmed by previous research in our group [23]. An thermal finite element simulation was conducted to characterize the temperature distribution in the device. The temperature sensing capability of an embedded p–n diode/p-probe temperature sensor system was experimentally characterized and correlated with finite element simulation.

The paper is organized in the following way. The next Section 2 introduces in brief the fabrication processing steps of thermal microprobe device. Section 3 describes analytical method to estimate probebase. Section 4 presents details on the finite element modeling of the device. Section 5 presents conducted experimental results with fabricated micro-probe. Section 6 provides discussion about obtained results from computation and experiment. Finally, Section 7 summarizes conclusions.

2. Fabrication process

Silicon micro-probe array was fabricated as follows. Firstly, a silicon dioxide (SiO_2) thin film layer of 860 nm was grown by standard dry thermal oxidation at 1273 K and annealed in N_2 atmosphere. Next, the oxide layer was patterned by buffered hydrofluoric acid (BHF) followed by deposition of catalytic Au film of 200 nm on (111) n-Si substrate (resistivity of 3–6 Ω-cm) (Fig. 1(a)).

The substrate was heated at 973 K for a few minutes resulting in a hyper-eutectic Au–Si alloy between the Au film and the Si substrate. Then, a vapor–liquid-solid (VLS) growth technique [23,24] was employed to grow vertical probe array using molecular beam epitaxy (MBE) process in a chamber with the following growth condition: Si_2H_6–B_2H_6 gas mixture at a pressure of 0.6 Pa, B_2H_6 concentration of 8000 ppm (producing p-Si probe with a resistivity of 1 Ω-cm, substrate temperature of 973 °C, and duration of 25 min (Fig. 1(c)). To be noted here is that during MBE growth process of Si probes, a poly-silicon layer of 1 μm was formed, which has significantly lower thermal conductivity than the crystalline silicon due to phonon scattering grain boundaries. This auto deposited poly-Si layer was patterned by etching with XeF_2.

Next, a silicon dioxide (SiO_2) insulation layer of 600 nm was deposited using plasma enhanced chemical vapor deposition (PE-CVD) technique (Fig. 1(c)). To partially expose probe tips, a uniform layer of photoresist (>2 μm) was spray coated followed by projection printing technique to partially expose the probe tip without mechanically breaking the microprobe (Fig. 1(d)).

Finally, to produce interconnection, an aluminum (Al) layer of a 500 nm was formed over the probes by sputtering and lithographic technique (Fig. 1(e)). This technique thus adopted resulted to vertically grown (111) silicon micro-probes of 3 μm diameter and 30 μm in length with interspacing of 100 μm. Details can be found elsewhere [25].

As p-Si microprobe is fabricated on n-Si substrate, a p–n junction diode is formed which can be used as both temperature and force sensors. Henceforth, we will focus only on the temperature sensing capability of microprobes.

3. Analytical 1-D thermal model

As mentioned earlier, during the growth of p-silicon probes on an n-silicon substrate using VLS technique, the p–n diode system was inherently formed at the probe/substrate junction. The temperature dependent rectifying I–V curves of p–n diode can be utilized for temperature sensing with microprobe.

Assuming 1-D heat flow, the temperature, T_j at probe/substrate junction can be roughly estimated as

$$T_j = \frac{r_{\mathrm{sp}}+r_{\mathrm{su}}}{r_p+r_{\mathrm{sp}}+r_{su}}T_p + \frac{r_p}{r_p+r_{\mathrm{sp}}+r_{\mathrm{su}}}T_r \tag{14}$$

where r_p ($9.3\times10^{-3}\ K/W$), $r_{su}=\frac{t_{Si}}{k_{Si}A_{Si}}$ (with $k_{Si}=148$ W/m·K, $t_{Si}=325$ μm), and $r_{sp}=\frac{1}{k_{Si}2\pi L}tan^{-1}(\frac{2t_{Si}}{L})$ (with L = 5 μm, diameter of probe base) are thermal resistance of probe, thermal resistance of substrate, spreading resistance at the constriction of probe to substrate respectively. T_p and T_r (or T_a) are the tip temperature of the probe and the reference temperature. Fig. 2 shows an analytical model of the temperature sensing microprobe device.

Assuming $T_r = 293$ K, a simple calculation shows that for the temperature increase (T_j) of 1 K at the junction requires 290.5 K at the probe tip. This could be a significant overestimation because temperature dependent thermal conductivities (see Table 1), 3-D thermal fluxes in lateral direction and aluminum are neglected. 3-D finite element simulation is therefore necessary to address this shortfall.

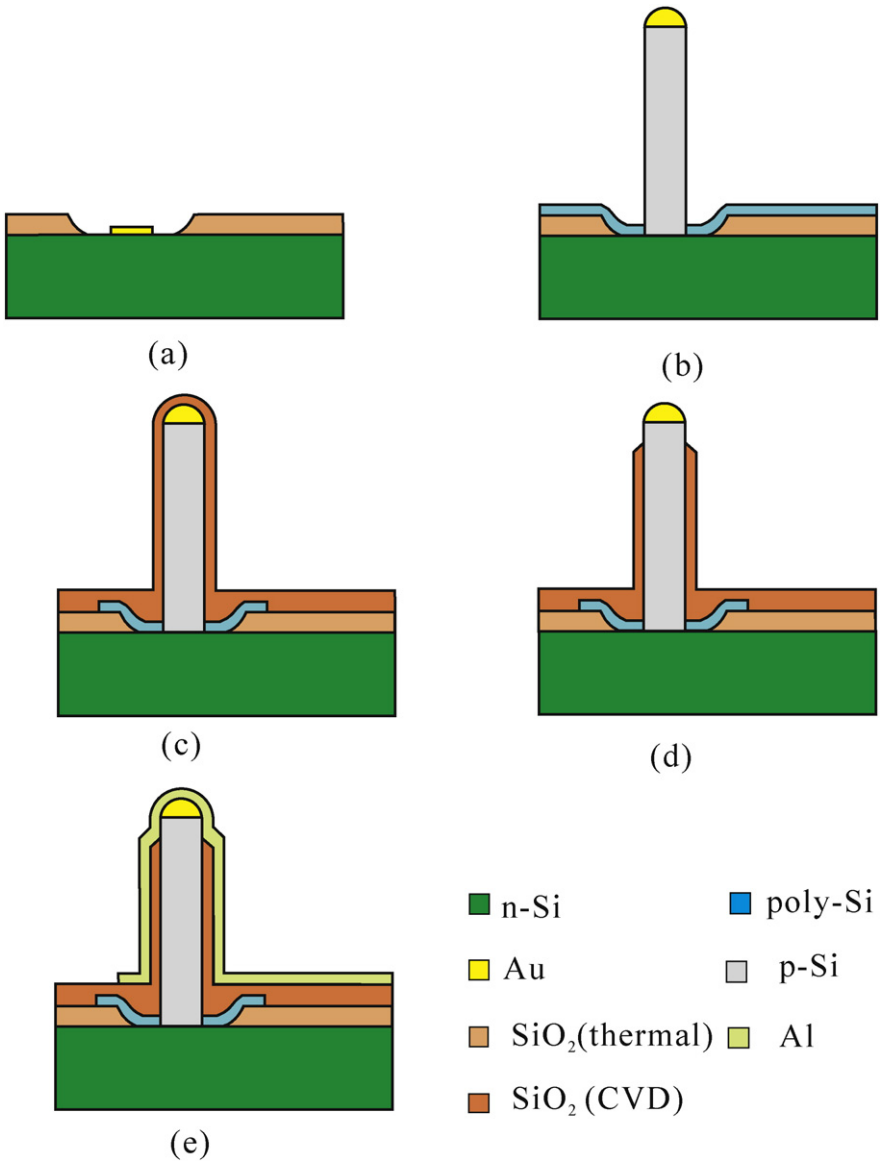

Fig. 1. Processing steps for the fabrication of micro-probe device: (a) deposition of Au thin film structure on a n-Si(111) substrate, (b) VLS growth of p-Si micro-probe array, (c) patterning of Poly-Si and deposition of SiO_2 insulator, (d) etching of SiO_2 to expose probe tip, (e) deposition of Al film for wiring and patterning.

4. Computation

3-D finite element model was constructed for micro-probe array device. Without any penalty in accuracy of thermal simulation results, one micro-probe with symmetric part of the substrate with periodic boundary conditions is sufficient to model.

Fig. 3(a) shows an overall view of meshes used for the model thus considered. For the purpose of 3-D visualization, a half of the device is rendered invisible (Fig. 3(b)). To reduce the number of elements in the model, coarser meshes were used in the regions where high thermal gradient was expected (especially in substrate). The software code Msc.Marc was used to perform FE computations [26].

Table 1 shows a summary of the material parameters i.e. thermal conductivity (k), specific heat (c), and mass density (ρ) used in simulations. Thermal conductivity (k) and specific heat (c) were treated in the model as a function of temperature (see footnote of the table). All the numbers in the footnote are valid with the respective SI units. The data presented in the table was calculated at 300 K.

3-D finite element model was constructed for the designed temperature sensing microprobe array. For this computationally huge model, a single microprobe with symmetric part of the substrate was modeled. In fist simulation, the tungsten needle was placed at 5 μm above the probe. In this configuration, the thickness of air is also 5 μm which is modeled taking surface elements of probe-tip and w-tip (immediately on top of the probe) for 3-D meshing.

Transient thermal behavior of the microprobe was numerically simulated. The following boundary conditions were used. A temperature of 373 K was applied to the W-needle and the bottom surface of silicon wafer was considered to be at room temperature (293 K). Heat conduction coefficient is calculated using Eq. (5) to account for the major heat conduction path in air from W-tip to probe. Convective heat transfer has secondary effect at microscale thus plays a role too. Therefore, convective heat transfer coefficient is calculated using Eq. (12) and convection boundary condition is applied to air in-between probe and needle. A radiative heat boundary condition was applied to take into account the thermal radiation between the two surfaces of W-needle and Si-probe following Eq. (13). Fig. 4 shows the obtained results from simulation.

Fig. 5(a) shows a path-plot of temperature variation at the location of embedded p–n diode. A temperature increase of 1.4 °C was obtained from computation. The temperature gradient along the centre-line of the probe is presented in Fig. 5(b).

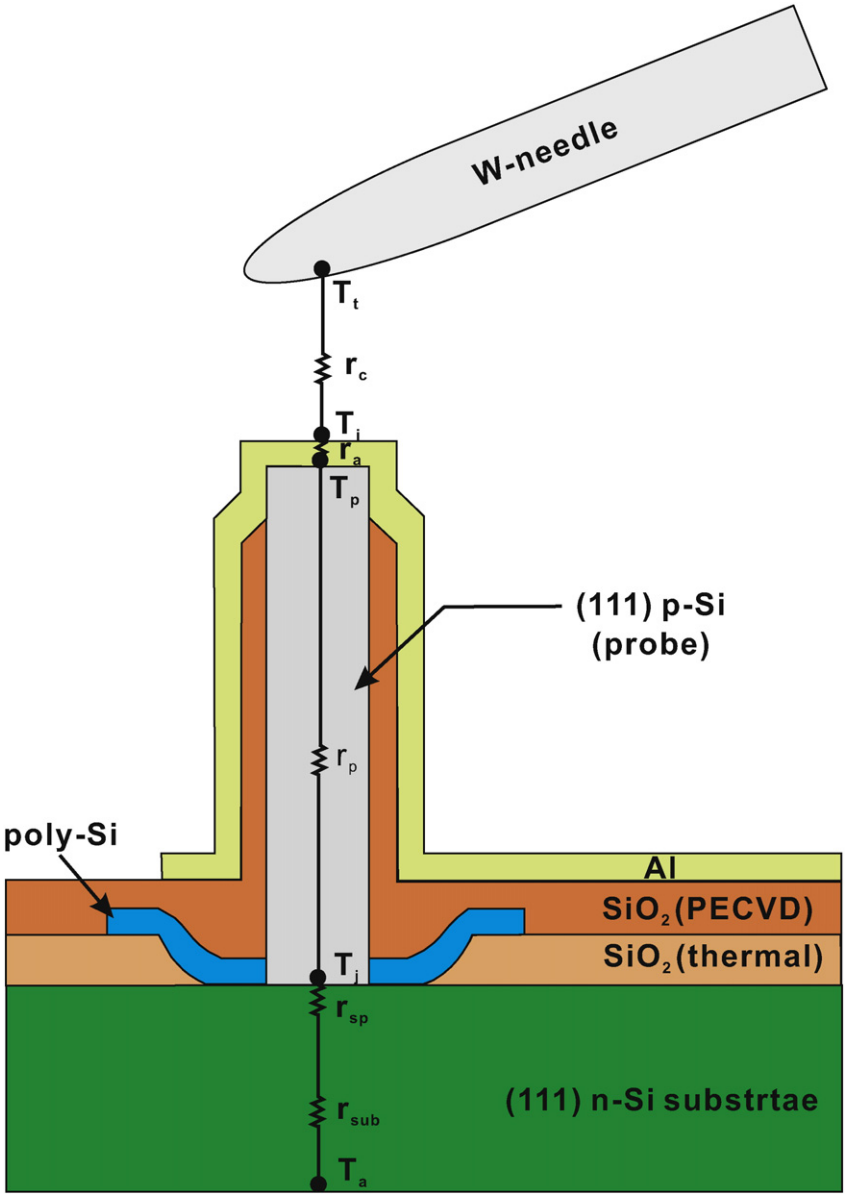

Fig. 2. 1-D thermal model: T_t, T_i, are temperatures at W-tip and Al-tip respectively, r_c, r_a are thermal resistance in air (or contact thermal resistance when w-tip is in contact with the probe) and thermal resistance in Al respectively (other notations are explained in the text).)

5. Experiment

W needle with tip diameter of 1 μm was used to mimic a hot object to sense with the fabricated microprobe. To heat the W needle, it was attached to four heating resistors ($4 \times 12.5 = 50\ \Omega$) with a good thermal conductive silver paste (Fig. 6(a)). These resistors and W needle were electrically insulated. By applying 12.0 V, 223 mA to these resistor, the W needle was heated by Joule heating and a temperature difference of 80 K with respect to ambient temperature (293 K) was determined by thermography (TH5100, NEC Avid infrared Technologies Co., Ltd.) on the needle marked with black ink. The heated W needle was fixed to an electrically insulating and thermally stable bamboo chopstick, which was then mounted on a manipulation system to precisely control the position of the W needle on the microprobe.

To experimentally measure the temperature sensitivity of p–n diode, the fabricated sensor was placed on a thermal stage in a dry N_2 atmosphere. For a temperature increase (ΔT) of 50 K, I–V characteristics were captured at 10 K intervals. The temperature thus increase resulted in decreasing built-in potential of the p–n diode and thereby, shifted the rectifying I–V curves of p–n diode negatively. The temperature sensitivity of the p–n diode was measured to be −2.3 mV/K (at 0.1 μA) which agrees well with that of values for silicon p–n diodes (−0.1 to −0.3 mV/K) [15].

Next, the measurement system was placed in a dark shielded box. Using a dedicated manipulator the heated W needle was placed on the tip of the microprobe at different manipulation heights, z: 5 μm (above the probe tip), 0 μm (just touching the probe tip), 2 μm (compressed down on the probe tip), 4 μm (compressed down on the probe tip), and 6 μm (compressed down on the probe tip) and voltage was varied from 0.19 to 0.25 V. The applied voltage was lower than the threshold voltage, +0.4 V of the p–n diode thus eliminating any piezoresistive influence in I–V characteristics (see Fig. 6(b)).

Fig. 6(c) shows the shift of I–V curves due to placing of W needle at different manipulation heights. The quantified shift of curves were found to be −3.0 mV (for z 5 to 0 μm), −7.9 mV (for z 0 to 2 μm), −15.3 mV (for z 2 to 4 μm), and −25.7 mV (for z 4 to 6 μm). Using the measured temperature sensitivity of the p–n diode, the above shift

Table 1
Thermal–physical properties of materials.

Material	Thermal conductivity, k [$Wm^{-1}K^{-1}$]	Specific heat, c [$J\,kg^{-1}K^{-1}$]	Density, ρ [$kg\,m^{-3}$]
Air	0.026 [27]	1006[c]	1.18[c]
Si[a]	150 [28]	700 [27]	2330[c]
Si[b]	32 [29]	705[c]	2330[c]
SiO_2	1.38[c]	745[c]	2220[c]
Al	237 [30]	897 [30]	2702[c]
W	174[c]	132[c]	19,300[c]

$k_{air}=3.9539e^{-4}+9.886e^{-5}T-4.367e^{-8}T^2+1.301e^{-11}T^3$. [31]
$k_{Si}=696.7-2.8325T+3.345e^{-3}T^2$.
$k_{p-Si}=-2.2e^{-11}T^3+9.0e^{-8}T^2-1e^{-5}T+0.014]^{-1}$. [32]
$k_{SiO_2}=696.7-2.8325T-3.345e^{-3}T^2$.
$k_{Al}=246-0.075T+1.5e^{-4}T^2$.
$k_W=201-4.5e^{-2}T-1.5e^{-4}T^2$.
$c_{Si}=10+3.51T-3.9e^{-3}T^2$.
$c_{SiO_2}=265+1.6T$.
$c_{Al}=411+2.525T-2.95e^{-3}T^2$.
$c_W=87+0.225T+2.5e^{-4}T^2$.
[a] Single crystal.
[b] Polycrystal.
[c] [33].

of I–V curves corresponds to the temperature rise of 1.3, 3.4, 6.7, and 11.2 K respectively.

Table 2 presents a comparison between experimentally and computationally obtained temperature rise, ΔT. In simulation, it is assumed that when W-needle just touches the microprobe about 25% area of its tip had microcontact and remaining area had air-gap. Similarly, when W-needle pressed against the microprobe (2 μm through manipulator) 50% area of its tip had microcontact and the rest had air-gap. When W-needle pressed against the microprobe (4 μm through manipulator) 100% area of its tip had microcontact thus air-gap was nil based on the experimental finding that thee was no change in ΔT at both 4 μm and 6 μm manipulator heights.

6. Discussion

Heat transfer mechanism in microprobe is somewhat complicated. Heat conduction in silicon is mainly governed by phonon transport mechanism even with high dopant concentrations. Thermal conductivity in p-type silicon used for fabrication of microprobe may significantly be reduced due to doping impurity concentration compared to its bulk counterpart. The crystallographic orientation of probe may also influence its thermal conductivity. The anisotropic heat conduction, in silicon at low temperatures was measured to be 32 W m^{-1} K^{-1} which is significantly smaller than that of its bulk counterpart of 150 W m^{-1} K^{-1} [28,29].

In Fig. 6(c) the negative manipulation height, z indicates compression of the W-needle on microprobe. When z was set to be 0 or 2 μm, the temperature rise (ΔT) was just 3 or 5 times higher than that

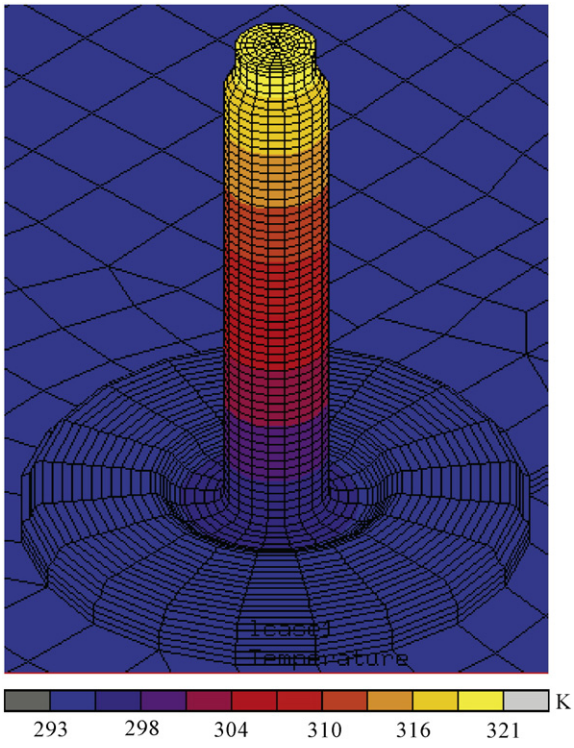

Fig. 4. Temperature distribution (3D-model) on a single microprobe with 3 μm probe diameter and 30 μm probe height.

obtained with z (5 μm). This can be attributed to microscale heat conduction to the probe and p–n diode which is limited by the thermal contact resistance between the W-needle and the microprobe. Further increasing z moves the W-needle further downward with a significant reduction in the thermal contact resistance resulting in good heat conduction to the silicon microprobe which is attributed to the shift in the I–V curves (see Table 2). However, for stronger contact forces with z = 4 and 6 μm, ΔT remains constant implying negligible thermal contact resistance where heat conduction (to the p–n diode through the microprobe) is limited by the thermal resistance of the silicon microprobe element. Therefore, thermal contact resistance (r_c) depends on air-gap thickness. As the experiment was conducted at a constant temperature of W-needle, it was not possible to investigate its temperature dependency. Using Eqs. (2), (5), (12), and (13), a typical thermal contact resistance was calculated to be 107.4 K/W assuming that asperity height is 1 μm (based on a secondary electron microscopy (SEM) of probe tip) and 50% of total probe tip area had air pockets when manipulation height, z = 0 i.e. W-needle just touched the probe. However, this research can be further extended to capture SEM image (and asperity height map by 3-D Optical Microscopy) after each step of changing

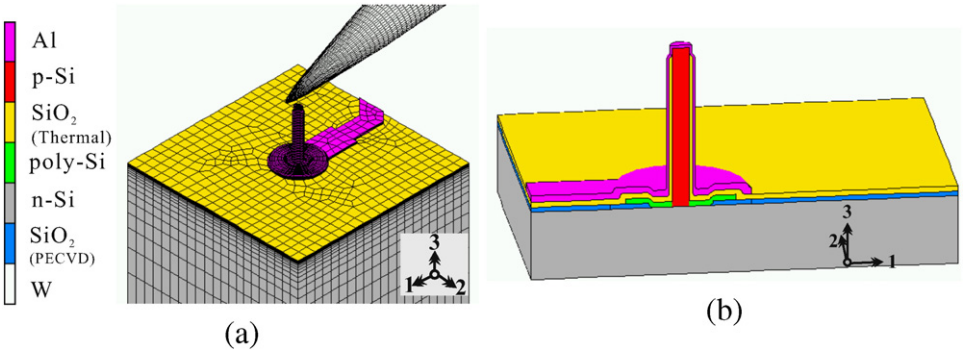

Fig. 3. (a) 3-D model depicting mesh details of micro-probe device (for visualization purpose, parts of W-needle and Si-substrate are made invisible) and (b) a cross-sectional view the device.

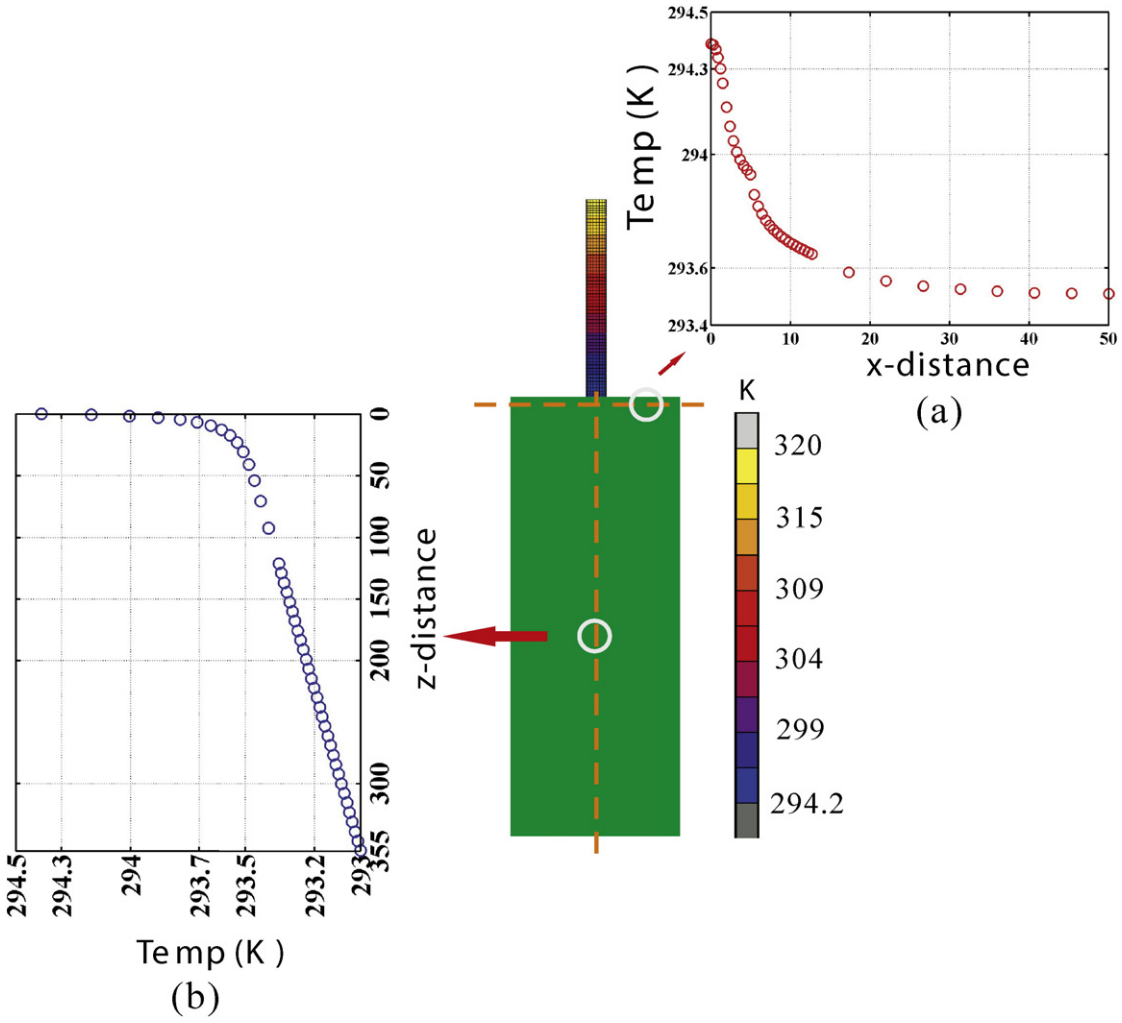

Fig. 5. Computational results of temperature distribution and temperature locality at the vicinity of p–n diode (when W needle was positioned at 5 μm above the probe-tip): (a) temperature profile along a horizontal line at p–n junction, and (b) along a vertical line through the wafer from the base of microprobe.

manipulation height. This would necessitate high speed computing with dedicated server to incorporate microscopic features with very fine mesh.

The temperature gradient (dT/dx) obtained from Fig. 5(a) shows that the localized temperature gradient tends to zero at the spatial distance of about 40 μm from the centre of the probe. Thus, the interspacing of 100 μm between neighbored probes is proved to be sufficient to get rid of influence from nearby probes (cross-talk). While conducting experiment, the whole system was placed on top of an aluminum block thereby allowing to consider ambient temperature boundary condition at the bottom of sensor device.

The mean free path of air molecules is about 60 nm [34]. Considering different air-gap heights between W-needle and Si-probe, one would find different Knudsen numbers, *Kn* manifesting non-continuum effects in three regimes (Eqs. (9), (10), and (11)). Even, when the W-tip touches Si-probe meniscus of air (nano-scale) may exist due to interface roughness particularly of Si-probe tip. This is expected to effect non-continuum thermal conduction phenomena in transition or free-molecular region as air-gap size would be the same order of magnitude that of the mean free path of air molecules.

Moreover, to capture thermal response using microprobes it is important to investigate thermo-mechanical reliability of sensing devices. We have simulated thermo-mechanical integrity of device structure which is beyond the scope of this paper.

7. Conclusions

Employing both computational and experimental techniques, microscale heat transfer has primarily been investigated for fabricated p-silicon microprobe array. p-Silicon microprobes with embedded p–n diodes on n-silicon substrate demonstrated as a novel temperature sensor that can be used for many prospective applications such as artificial electronic fingertips of a robot-hand/prosthetics to sense of touching temperature and temperature mapping to investigate small materials including biological soft samples. Finite element simulations were conducted to probe microscale temperature with p-silicon microprobe/p–n diode array. For small manipulation heights, the heat conduction is limited by the thermal contact resistance between the W-needle tip and the microprobe tip. In contrary, for higher manipulation heights, heat conduction to the p–n diode through the silicon microprobe is limited by the thermal resistance of the silicon microprobe element. FE model thus can be used as a tool for a priori justifying the functionalities of temperature sensor with uniaxially grown vertical microprobe array.

Acknowledgments

This research was conducted under the Global COE program “Frontiers of Intelligent Sensing” of Toyohashi University of Technology

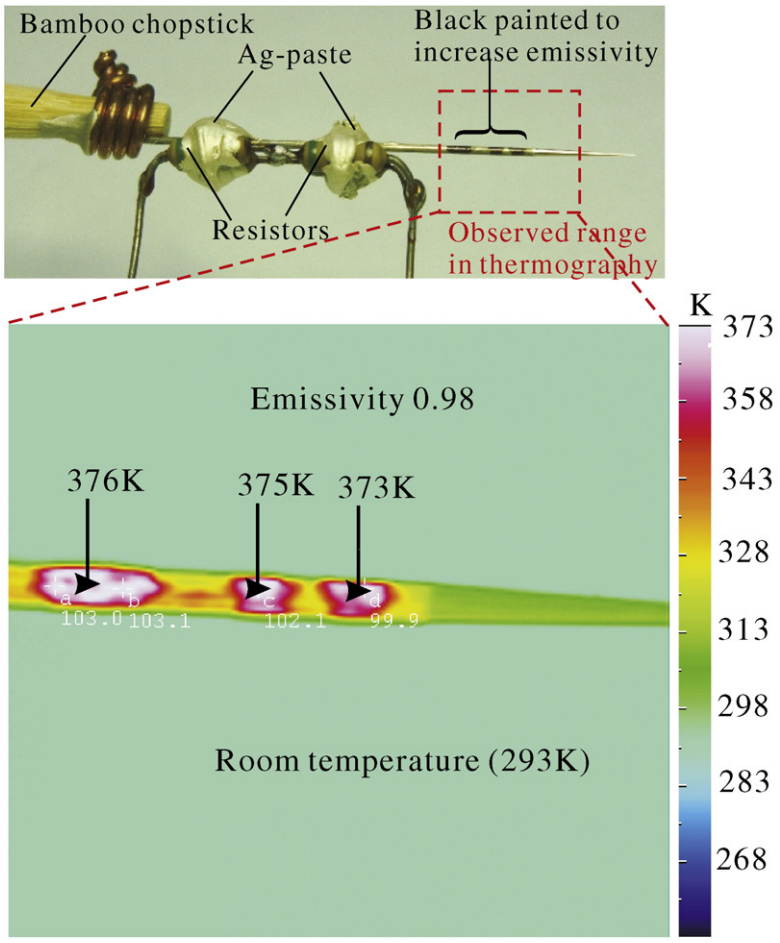

(a)

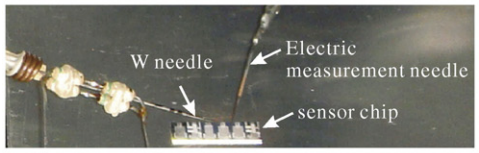

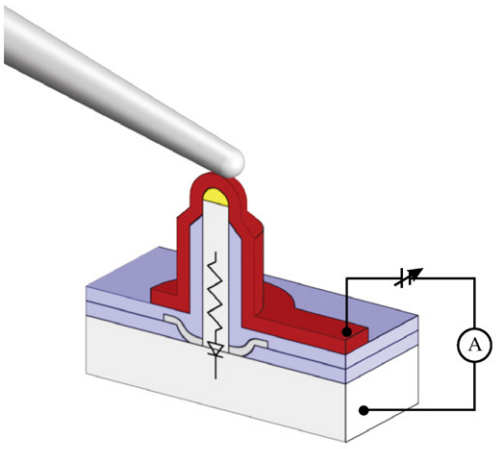

(b)

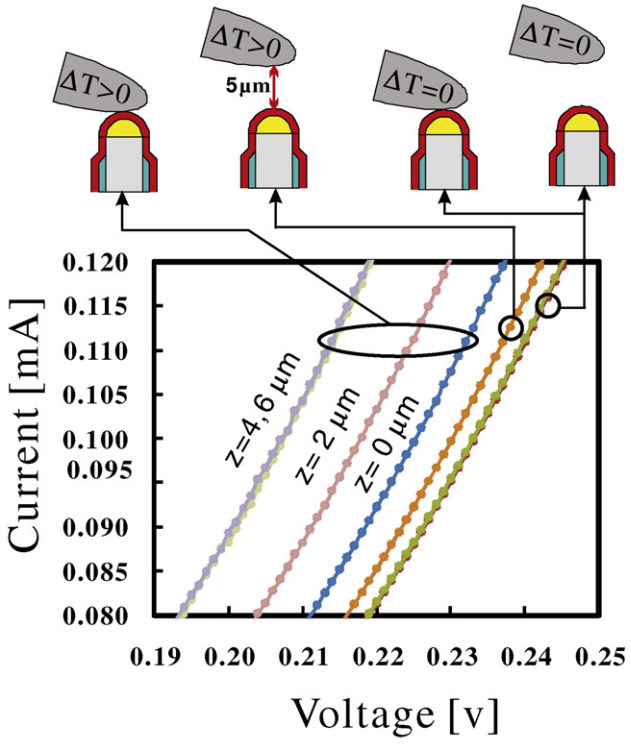

(c)

Fig. 6. Experiments with temperature sensor: (a) temperature distribution obtained from thermography, (b) thermal sensing measurement set-up, and (c) shifting of I–V curves.

Table 2
Comparison of temperature rise, ΔT (at p–n diode) obtained from FEM computation and experiment.

Manipulation height	Temperature rise ΔT [K]	
h [μm]	Experiments	Computations
5 (W-tip is above the Si-probe)	1.3	1.4
0 (W-tip just touches Si-probe)	3.4	3.6
2 (W-tip compresses Si-probe)	6.7	7.9
4 (W-tip compresses Si-probe)	11.2	12.2
6 (W-tip compresses Si-probe)	11.2	–

(TUT) from the Ministry of Education, Culture, Sports, Science and Education, Japan.

References

[1] T. Kawano, Y. Kato, M. Futagawa, H. Takao, K. Sawada, M. Ishida, Fabrication and properties of ultra small Si wire arrays with circuits by vapor–liquid-solid growth, Sensors Actuators A 97 (2002) 709–715.
[2] T. Kawano, H. Takao, K. Sawada, M. Ishida, Multichannel 5 × 5-site 3-dimensional Si micro-probe electrode array for neural activity recording, Jpn. J. Appl. Phys. 42 (2003) 2473–2477.
[3] T. Kawano, Y. Kato, R. Tani, H. Ishino, H. Takao, K. Sawada, M. Ishida, Neuron size Si probe array fabricated on integrated circuits for multichannel electrode, Proc. 12th Int. Conf. Solid-State Sensors and Actuators (Transducers'03) 2003, pp. 1679–1682.
[4] M. Ishida, T. Kawano, M. Futagawa, Y. Arai, H. Takao, K. Sawada, A si nano-micro-wire array on a Si(111) substrate and field emmisison device applications, Superlattice. Microst. 34 (2003) 567–575.
[5] K.E. Jones, P.K. Compbell, R.A. Normann, A glass/silicon composite intracortical electrode array, Ann. Biomed. Eng. 20 (1992) 423–437.
[6] M.D. Gingerich, J.F. Hetke, D.J. Anderson, K.D. Wise, A 256-site 3D CMOS microelectrode array for multipoint stimulation and recording in the central nervous system, Proc. 11th Int. Conf. Solid-State Sensors and Actuators (Transducers'01) 2001, pp. 416–419.
[7] D.A. Robinson, The electrical properties of metal microelectrodes, Proceeding of the IEEE, vol. 56 1968, pp. 1065–1071.
[8] R.A. Normann, Microfabricated electrode arrays for restoring lost sensory and motor functions, Proc. 12th Int. Conf. Solid-State Sensors and Actuators (Transducers'03) 2003, pp. 959–962.
[9] N. Sato, K. Machida, H. Morimura, S. Shigematsu, K. Kudou, M. Yano, H. Kyuragi, MEMS fingerprint sensor immune to various finger surface conditions, IEEE Trans. Electron Device 50 (2003) 1109–1116.
[10] R.S. Wagner, W.C. Ellis, Vapor–liquid-solid mechanism of single crystal growth, Appl. Phys. Lett. 4 (1964) 89–90.
[11] A. Goryu, A. Ikedo, M. Ishida, T. Kawano, Nanoscale sharpening tips of vapor liquid–solid grown silicon microwire arrays, Nanotechnology 21 (125302) (2010) 1–5.
[12] M.O. Heuschkel, M. Fejtl, M. Raggenbass, D. Bertrand, P. Renaud, A three-dimensional multi-electrode array for multi-site stimulation and recording in acute brain slices, J. Neurosci. Methods 114 (2002) 135–148.
[13] H. Oka, K. Shimonoa, R. Ogawaa, H. Sugihara, M. Taketani, A new planar multielectrode array for extracellular recording: application to hippocampal acute slice, J. Neurosci. Methods 93 (1999) 61–67.
[14] C.S. Smith, Piezoresistance effect in germanium and silicon, Phys. Rev. 94 (1954) 42.
[15] S. Middelhoek, S.A. Audet, Silicon Sensors, Academic Press, London, 1989.
[16] P.H. James, F.I. Thomas, Advances in Heat Transfer, Academic Press Inc., New York, 1965.
[17] G.K. Ovrebo, Thermal simulation of four die-attach materials, Army research laboratory, Report-ARL-MR-0686, 2008.
[18] M.H. Han, X.G. Liang, Z.A. Tang, Size effect on heat transfer in micro gas sensors, Sensors Actuators A 120 (2005) 397–402.
[19] F.M. Devienne, Low density heat transfer, in: J.P. Hartnett, T.F. Irvine Jr. (Eds.),Advances in Heat Transfer, 2 1965, pp. 271–356.
[20] Z.M. Zhang, Nano/Microscale Heat Transfer, McGraw-Hill, New York, 2007.
[21] S.W. Churchill, Correlating equations for laminar and turbulent free convection from a horizontal cylinder, Int. J. Heat Mass Transf. (1975) 1049–1053.
[22] ASHRAE, ASHRAE handbook of fundamentals, vol. 8, ASHRAE, Atlanta, 1993.
[23] M. Ishida, K. Sogawa, A. Ishikawa, M. Fujii, Selective growth of Si wires for intelligent nerve potential sensors using vapor–liquid-solid growth, Proc. 10th Int. Conf. Solid-State Sensors and Actuators 1999, pp. 866–869.
[24] A. Akihito Ikedo, T. Kawashima, T. Kawano, M. Ishida, Vertically aligned silicon microwire arrays of various lengths by repeated selective vapor–liquid-solid growth of n-type silicon/n-type silicon, J. Micromech. Microeng. 95 (033502) (2009) 1–3.
[25] A. Ikedo, M. Ishida, T. Kawano, Out-of-plane high-density piezoresistive silicon microwire/pn diode array for force- and temperature-sensitive artificial whisker sensors, J. Micromech. Microeng. 21 (035007) (2011) 1–7.
[26] http://www.mscsoftware.com/product/marc.
[27] L. Lin, M. Chiao, Electrothermal responses of lineshape microstructures, Sensors Actuators A 55 (1996) 35–41.
[28] N.D. Mankame, Modeling of electro-thermalcompliant mechanisms(M.S. Thesis) University of Pennsylvania Philadelphia, PA, 2000.
[29] Y.C. Tai, C.H. Mastrangelo, R.S. Muller, Thermal conductivity of heavily doped LPCVD polycrystalline silicon films, J. Appl. Phys. 63 (1988) 1442–1447.
[30] F. Solzbacher, A new SiC-HfB_2 based micro hotplate for metal oxide gas sensors(PhD Thesis) Der Fakultät Elektrotechnik und Informationstechnik der Technischen Universität Ilmenau, 2003.
[31] R.P. Manginell, Polycrystalline-silicon microbridge combustible gas sensor(Ph.D Thesis) University of New Mexico, Albuquerque, NM, 1997.
[32] C.D. Lott, Electrothermomechanical modeling of surface-micromachined linear displacement microactuator(M.S. Thesis) Brigham Young University, Provo, Utah, 2001.
[33] F.P. Incropera, D.P. DeWitt, Fundamentals of heat and mass transfer, Wiley, New York, 2002.
[34] W. Rohsenow, H. Choi, Nano/Microscale Heat Transfer, Prentice-Hall, Englewood Cliffs, NJ, 1961.